

THE CHANDRA IRON-L X-RAY LINE SPECTRUM OF CAPELLA

Ehud Behar, Jean Cottam, and Steven M. Kahn

*Columbia Astrophysics Laboratory, Columbia University, New York, NY 10027-5247*¹

An analysis of the iron L-shell emission in the publicly available spectrum of the Capella binary system, as obtained by the High Energy Transmission Grating Spectrometer on board the Chandra X-ray Observatory, is presented. Almost all of the spectral lines in the 10 – 18 Å wavelength range are identified. It is shown that, for the most part, these lines can be attributed to emission from L-shell iron ions in the Capella coroneae, namely from charge states Fe^{15+} to Fe^{21+} . It is also shown that the observed spectrum can be reproduced by assuming a single electron temperature of $kT_e = 600$ eV and single electron density for the iron-L emitting regions. It is demonstrated, however, that for electron densities below 10^{13} cm^{-3} , the intensity ratios of iron L-shell lines between 10 and 18 Å are essentially independent of the density and therefore are not useful for density diagnostics. The fractional ion abundances for Fe^{15+} to Fe^{21+} are derived from the spectrum and found to be: 0.06, 0.34, 0.25, 0.13, 0.11, 0.06, and 0.05, respectively. The comparison of these abundances with ionization balance calculations in the literature also indicates a temperature of about 600 eV, which is very similar to the temperature derived from line ratios within charge states. Finally, a volume emission measure of $2 \times 10^{53} \text{ cm}^{-3}$ is calculated for the iron L-shell emitting regions of the Capella coroneae.

Subject headings: atomic processes --- line: identification --- x-rays: stars --- stars: individual (Capella)

¹ E-mail addresses: behar@astro.columbia.edu, jcottam@astro.columbia.edu, skahn@astro.columbia.edu,

1. INTRODUCTION

The Capella binary system consists of well-separated G1 III and G8 III stars with an orbital period of 104 days (Hummel et al. 1994). Being one of the strongest coronal x-ray sources in the sky, Capella has been observed with all of the available x-ray telescopes dating back to the 1970's (Catura, Acton, & Johnson 1975). Past investigations, prior to the launch of the Chandra X-Ray Observatory, have been based upon limited-resolution broadband measurements. The present spectrum, which has been made publicly available in conjunction with the Chandra Emission Line Project (Brickhouse & Drake 1999), was obtained with the High Energy Transmission Grating (HETG) spectrometer on board Chandra (Markert et al. 1995) as part of the HETG calibration program. It features many resolved spectral lines, and provides a much more detailed insight into Capella's coronae than previous observations. Along with the Low Energy Transmission Grating (LETG) observation of Capella presented by Brinkmann et al. (2000), these are the first observations of this quality from stellar coronae, apart from the well-studied solar corona. By comparing the observed spectrum with detailed calculated spectra at various plasma conditions, we attempt to provide a better understanding of the Capella coronae and of the atomic processes that are responsible for the strong x-ray line emission.

Similar to the spectrum of the Sun, the Capella x-ray spectrum is dominated by numerous iron L-shell emission features accompanied by a few K-shell lines from other elements, such as oxygen, neon, magnesium, and silicon. As in many iron-rich astrophysical plasmas, the strong lines emitted by the highly abundant Ne-like Fe^{16+} ion are the most prominent lines in the Capella x-ray spectrum. These lines have been predicted to be promising candidates for temperature diagnostics in hot plasmas (Raymond & Smith 1986). The temperature dependence of the collisional excitation rates from the ground state $2p^6$ to the excited configurations $2p^53s$, $2p^53d$, and $2p^54d$ is expected to be particularly useful. The radiative decays following these excitations result in well-resolved x-ray lines around 17, 15, and 12 Å, respectively. The advantage of these lines as diagnostic tools is that they all pertain to a single ionization state and therefore the analysis of their intensities is independent of the ionization balance calculations, which strongly rely on total ionization and recombination rate coefficients that are probably of questionable accuracy.

Most of the previous studies of Capella have concluded that its spectrum is comprised of two or more temperature components. The low- and high- temperature components have been interpreted as arising from smaller and larger coronal loops (Mewe et al. 1982 and Vedder & Canizares 1983). Different plasma emission models have been employed to explain the observed spectrum and emission measure as a function of the two temperature components by best-fit methods. The ionic fractional abundances for the various elements were incorporated in these models from the literature (e.g., Arnaud & Raymond 1992). A few models also allowed the elemental abundances to vary from their solar values. The spread of temperatures found from the different missions and by the various methods is larger than can be explained by observational uncertainties. These temperatures range from 130 eV and 680 eV by Bauer & Bregman (1996) to 400 eV and 1900 eV by Lemen et al. (1989). However, the large discrepancies are not too surprising if one takes into account the variety of codes and the high number of free parameters in the fitting procedure.

In addition to the temperature, there have been previous measurements of the electron density in the Capella coroneae, mostly by using ratios of EUV lines originating from iron L-shell ions. Linsky et al. (1998) obtained the high electron-density value of a few times 10^{12} cm^{-3} , which is not inconsistent with the $4 \times 10^{11} - 10^{13} \text{ cm}^{-3}$ estimation by Dupree et al. (1993). In the solar corona, such high densities have been detected only during flares (Feldman & Doschek 1978 and Feldman, Doschek, & Kreplin 1982). There is no direct evidence for intense flaring activity in Capella. Brinkman et al. (2000) have recently employed He-like line ratios of carbon, nitrogen, and oxygen to measure an electron density between 10^9 and 10^{10} cm^{-3} for Capella. However, these low-Z ions are most likely formed at different coronal regions than the iron L-shell ions. To the best of our knowledge, x-ray lines from iron L-shell ions do not provide density-sensitive line ratios for hot plasmas at densities below 10^{13} cm^{-3} . Only at higher densities do collisional excitation processes start playing an important role in altering the line intensities, especially by depleting the upper levels of forbidden lines. In order to correctly reproduce the line intensities for electron densities above 10^{13} cm^{-3} , the pure coronal approximation may not be sufficient. Instead, a more comprehensive collisional-radiative model, which includes the collisional transitions between excited levels, is needed.

In the present work, we focus on the spectrum of the Capella binary system in the wavelength range of 10 - 18 Å, as detected by the HETG spectrometer on board the Chandra X-Ray Observatory in August 1999. The well-resolved spectrum exhibits many individual spectral lines that were not resolved in earlier observations. The spectrum is matched with detailed level-by-level calculations, using the Hebrew University Lawrence Livermore Atomic Code (HULLAC) by Bar-Shalom et al. (1998), for seven charge states of iron, Fe^{15+} to Fe^{21+} , which allow us to construct theoretical spectra at different plasma conditions. One of the main goals of this work is to show that the atomic calculations can accurately reproduce the Capella spectrum in this wavelength range. Starting with the simplest model, we assume a single electron temperature and electron density for the entire ensemble of iron charge states. This highly simplifying assumption turns out to be fairly adequate within the observational uncertainties of the present spectrum. The theoretical spectra together with the theoretical line ratios are calculated by using a collisional-radiative model for each ionization state. By fitting the lines from each charge state separately, we avoid the inaccuracies involved in computations of ionic fractional abundances. On the other hand, by fitting the theoretical spectra obtained for several charge states of iron to the multi-ion observed spectrum, the empirical fractional abundances of the iron ions can be derived and compared with theoretical results from the literature. In the last part of this paper, a volume emission measure is calculated for the iron-L emitting regions of the Capella coroneae.

2. OBSERVED SPECTRUM AND LINE IDENTIFICATION

Capella was observed on August 28, 1999 for 14.8 ks as part of the HETG calibration program. The standard Chandra X-ray Center (CXC) processing produced event-reconstructed and aspect-corrected data for the publicly available Chandra archive in the form of ‘fits’ files. We have post-processed these files using custom software to extract the spectra. The CXC aspect correction algorithm had left a ghosted image (170 seconds), which was removed from the data set. A spatial filter 30-pixels wide was applied along the images of both the Medium Energy Grating (MEG) and the High

Energy Grating (HEG) to separate the two spectra. For each of these data sets, the events were then plotted in dispersion versus pulse-height space to separate the spectral orders. A second filter, optimized interactively using a simple CCD model, selected all events associated with each order. The events were then plotted in a histogram with 5 mÅ bins.

The wavelength calibration was performed by first locating the zero-order centroid and then converting dispersion in pixel number to dispersion in wavelength, using the HETG geometry. The Advanced CCD Imaging Spectrometer (ACIS) chip gaps had not been included in the CXC pipeline when this observation was processed, and so they had to be determined by simultaneously optimizing the wavelength residuals between the positive and negative spectral orders for both the MEG and HEG. After this calibration process the wavelength uncertainty is ± 2 mÅ.

In order to determine the flux, the histogrammed spectra were divided by the ground-calibration effective-area curves that were reported by Schulz et al. (1999). A comparison of the resulting positive and negative first order flux for the MEG grating shows an agreement of 20% (or better) from 7 to 18 Å. This confirms the shape of the effective area curves and hence the relative flux across this wavelength band. These two spectral orders, which include the vast majority of the photon counts, have been added to improve the statistical reliability. Henceforth, the sum of these two orders will be referred to as the Capella spectrum. This spectrum in the 10 - 18 Å wavelength range is represented by the upper trace in Figs. 1a and 1b.

In order to facilitate the identification of this rich line spectrum, calculations have been performed for the iron ions Fe^{15+} through Fe^{21+} . All of the prominent lines in the 10 - 18 Å wavelength band of the Capella spectrum are identified, as well as most of the weak ones. The majority of the lines originate from iron L-shell ions, but a few oxygen, neon and nickel lines are also identified. In addition to the present HULLAC calculations, the most useful references for identifying the lines are the solar observation by McKenzie et al. (1980) and the comprehensive Electron Beam Ion Trap (EBIT) iron measurements by Brown et al. (1998, 2000). The theoretical spectrum, calculated for iron only, is plotted in Figs. 1a and 1b below the observed spectrum. The details of the calculations are discussed below in Sec. 4. The ranges corresponding to the most important types of transitions for the various iron ions are indicated above the spectrum. The individual line identifications are presented in Table I for the most prominent lines in accordance with the peak labels (first column) in Figs. 1a and 1b. In cases where a spectral feature is identified as a blend of several lines, all of these lines are listed in the table. The second column in Table I shows the wavelengths in Ångströms measured in the present observation ($\lambda_{\text{observed}}$). The third, fourth, and fifth columns, respectively, give the wavelengths previously measured in the Sun (λ_{Sun}), with EBIT (λ_{EBIT}), and the wavelengths presently calculated with the HULLAC code (λ_{HULLAC}). The following columns indicate the emitting ion and the upper and lower configurations of the radiative transition, including the total angular momentum quantum numbers of the relevant levels (J_U and J_L). It should be stressed that the actual atomic levels involved in the radiative process may be composed of components from more than one configuration (i.e., configuration mixing). In those cases, the configuration given in Table I represents the configuration of the major component of the level. The last column gives the measured flux from each line. For the very weak features, for which Gaussian fits were not obtainable, only a centroid wavelength is included with no flux.

It can be seen that for most of the strong lines, the presently observed wavelengths are in excellent agreement with those measured in the Sun and in EBIT. A few lines, which were not identified by McKenzie et al. (1980), are identified here. In general, the present line emission from Capella and the solar spectrum (McKenzie et al. 1980) feature many similarities, possibly implying that the outer atmospheres of Capella and the Sun may have much in common. In the EBIT experiments also, the numerous iron lines have been identified with the aid of HULLAC calculations. The accuracy of the HULLAC wavelengths is usually to within 10 - 20 mÅ. More importantly, it is the atomic transition rates that allow us to predict which lines (among thousands) will be observed in the spectrum and how intense will they be. In the following, we describe the atomic-state model as well as its application to the present Capella spectrum.

3. THE ATOMIC-STATE KINETIC MODEL

Coronal plasmas are characterized by relatively high temperatures and low densities, in which the most important atomic processes are electron impact excitations from the ground states and subsequent radiative decays, either directly to the ground states or via cascades. Coronal plasmas are usually, but not always, optically thin. In the present work, we use a full collisional-radiative steady-state model, which includes all the collisional excitations and de-excitations as well as all of the radiative decays between the levels of each ionization state, but neglects line self-absorption processes. The electron energy distribution is assumed to be Maxwellian, corresponding to an electron temperature T_e . The set of rate equations for the (time independent) density n_i^{q+} of an ion with charge $q+$ in a level i can be written as:

$$\frac{d}{dt} n_i^{q+} = n_e \sum_{j \neq i} n_j^{q+} Q_{ji}(T_e) + \sum_{j > i} n_j^{q+} A_{ji} - n_i^{q+} \left(n_e \sum_{j \neq i} Q_{ij}(T_e) + \sum_{j < i} A_{ij} \right) = 0 \quad (1).$$

A represents the Einstein rate coefficient for spontaneous radiative emission, and $Q(T_e)$ the rate coefficient for electron-impact excitation or de-excitation. The electron density is denoted by n_e . Level-by-level calculations have been carried out for each of the iron ions from Na-like Fe¹⁵⁺ through B-like Fe²¹⁺. For the various ions, high lying levels with n -values as high as 12, but not less than 6 (n being the principal quantum number of the excited electron) are included in the model. The set of equations (1) are solved by normalizing the sum of all level populations to unity. In other words, the population of each level is calculated in relation to the total population of ions in its ionization state. In the high-temperature and low-density limit, where collisional transitions between excited levels are negligible, this model reduces to the standard coronal model, which is sufficient for most of the present work. The line intensities in number of photons emitted per unit time and per unit volume are subsequently given by:

$$I_{ji} = n_j A_{ji} \quad (2).$$

All of the basic atomic quantities used in this work were obtained by means of the multi-configuration, relativistic HULLAC (Hebrew University Lawrence Livermore Atomic Code) computer package developed by Bar-Shalom et al. (1998). HULLAC includes the RELAC code for atomic energy levels (Klapisch et al. 1977) and for

radiative decay rates as well as the CROSS code for collisional excitation rate coefficients (Bar-Shalom, Klapisch, & Oreg 1988). The intermediate-coupling detailed level energies are calculated using the relativistic version of the parametric potential method by Klapisch (1971), including configuration mixing. The collisional rate coefficients are calculated in the distorted wave approximation, implementing the highly efficient factorization-interpolation method by Bar-Shalom et al. (1988).

4. RESULTS AND DISCUSSION

The individual spectrum for each of the ions Fe^{15+} through Fe^{21+} is obtained by a coronal model at a single electron temperature corresponding to 600 eV and at a single electron density of 10^{10} cm^{-3} . Each of these spectra is plotted separately at the bottom of Fig. 2. The isonuclear trends of the dominant 2p-3d transitions can be nicely seen in the figure shifting from about 15.0 Å for Fe^{15+} and Fe^{16+} to 11.8 Å for Fe^{21+} . Furthermore, the intensity of these transitions is shown to diminish with the ion charge as the number of electrons available for excitation in the 2p shell decreases. The theoretical spectral lines in Fig. 2 and throughout this paper are given a uniform Gaussian profile with 15 mÅ FWHM (Full Width at Half Maximum), slightly less than the observed line widths. The total iron spectrum is calculated by summing the contributions of all of the charge states. In this sum, each charge state is given a different weight corresponding to its ionic fractional abundance. The total calculated spectrum is normalized to the 2p-3d Fe^{16+} line at 15.264 Å. The fractional abundances are determined by fitting the relative line intensities of each ionization state to the observed intensities. The resulting fractions are indicated in the figure just above each individual-ion spectrum. The agreement between the Capella spectrum, given at the top of Fig. 2, and the total calculated spectrum, given just below it, can be seen to be very good. Note that the non-iron lines are not included in the theoretical spectrum. In particular, the discrepancy between the observed and calculated intensities usually does not exceed 20%, which is approximately the uncertainty of the measured flux. The largest discrepancies occur for the 2p-3s lines of Fe^{16+} and Fe^{17+} , which are about 30% too weak in our model. For better agreement, it may be advantageous to insert into the model experimentally measured wavelengths (e.g., Brown et al. 1998) and collisional excitation rate coefficients, where available.

The fact that the Capella x-ray spectrum is accurately reproduced with a single temperature does not necessarily imply that the entire Capella corone are isothermal, as it cannot be ruled out that longer wavelengths (up to EUV) are emitted from lower-temperature regions. Moreover, the present spatially and temporally integrated observation cannot be expected to reflect the temperature and density gradients nor the time variability that exist within the Capella corone. The present results, therefore, should be viewed as providing the most appropriate average temperature value for the iron-L emitting regions of the Capella corone. It should be further noted that Bauer & Bregman (1996) have successfully fitted a broadband (6 - 60 Å) spectrum of Capella measured by the ROSAT x-ray telescope, with a single temperature corresponding to 680 eV. Also, Vetter & Canizares (1983) showed that the spectrum of Capella measured by the Einstein Observatory, could be successfully modeled with a single-temperature of 540 eV. The present analysis of the high resolution HETG spectrum, however, constitutes a more detailed demonstration of the fact that one temperature and one density are sufficient for reproducing the iron L-shell x-ray spectrum of Capella, without any

assumptions regarding the ionization state of the plasma. In the determination of the ionic fractional abundances, the strongest 2p-3d line is used for each charge state, except for Fe^{16+} and Fe^{17+} , for which self-absorption may affect the observed line intensities. Instead, for these two ions, the other 2p-3d lines are used. Indeed, as can be seen from Fig. 2, the intensities of the strongest lines of Fe^{16+} and Fe^{17+} , at 15.015 Å and 14.206 Å, are overestimated in the calculations by about 30% and 10%, respectively.

The intensity ratio of the Fe^{16+} lines at 15.015 Å and at 15.264 Å has been a long-standing subject of numerous investigations. Brown et al. (1998) have measured this ratio in EBIT to be between 2.77 and 3.15 (depending on the electron beam energy), whereas the values from solar observations range from 1.5 to 2.4. The ratio measured in the present Capella spectrum is 2.4, fairly close to the measured value of 2.6 recently reported for Capella by Brinkmann et al. (2000). The low observed ratio has most frequently been attributed to self-absorption of the 15.015 Å line (e.g., Waljeski et al. 1994). The effect of self-absorption on the spectrum is rather difficult to calculate and can strongly depend on the geometry of the emitting plasma, which is only poorly known for the Capella coroneae. Here, we want to suggest another, perhaps complementary, explanation. Most investigators have overlooked the fact that the Fe^{15+} ion also has a very strong line close to 15.264 Å that blends with the Fe^{16+} line. This can be seen from the individual-ion spectra given in Fig. 2. The low values observed for the 15.015 Å / 15.264 Å ratio can therefore also be a consequence of the existence of Fe^{15+} in the plasma. For instance, the presently calculated ratio for Fe^{16+} alone gives a value of about 3.5 (the theoretical values have been shown by Brown et al. (1998) to overestimate the actual value by about 15%). However, in the total spectrum, where the Fe^{16+} and Fe^{15+} contributions have been added with the appropriate abundances, this ratio reduces by 10% to 3.15. At lower temperatures, where Fe^{15+} has a higher abundance, this ratio would be even smaller. In short, while the low values of the 15.015 Å / 15.264 Å line ratio, observed both in the Sun and in Capella, may or may not be due to self-absorption, they certainly are, at least partially, a consequence of line blending with Fe^{15+} .

4. PLASMA DIAGNOSTICS

4.1 Electron Temperature

A natural application of the present calculations is to employ the resulting line intensity ratios for plasma diagnostics. The relative intensities within each charge state of most of the iron lines in the currently studied wavelength range show only weak dependence on the electron temperature in the 200 eV to 1000 eV regime. This fact is demonstrated in Fig. 3, which gives the total calculated spectrum at a given density of 10^{10} cm^{-3} , but for three different temperatures, compared with the observed spectrum. All spectra are normalized to the 2p-3d line at 15.264 Å. In order to simplify the comparison, the fractional abundances best fit for 600 eV have been retained for the other temperatures as well. It can be seen that only minor differences occur between the various calculated spectra. As the temperature increases, the 2p-3d lines become slightly more intense with respect to the 2p-3s lines. However, not even the spectrum calculated for a temperature as low as 200 eV can fully explain the high intensity that is observed in Capella for the 2p-3s lines of Fe^{16+} and Fe^{17+} .

Perhaps the most easily observed temperature effect on the iron L-shell lines is the increasing intensity with temperature of lines originating from highly excited levels.

At low temperatures, the rates for collisional excitation to the high, upper levels of these transitions are very small. Only at higher temperatures, these levels become significantly populated. A good example for this is the 2s-3p line at 13.829 Å and the 2p-4d lines at 12.266 Å and 12.131 Å (all pertaining to Fe^{16+}). The mere fact that these lines are clearly seen in the Capella spectrum supports the hypothesis that the temperature is much higher than 200 eV. A similar temperature effect is predicted for the 2p-5d Fe^{16+} lines at 11.251 Å and 11.127 Å. Unfortunately, these lines in the present observation are either too weak or blended with other lines. This limits the accuracy expected from them as temperature diagnostics. Fig. 4 shows the calculated intensities for the 2s-3p line at 13.829 Å and for the 2p-4d line at 12.266 Å, with respect to the intensity of the 2p-3d line at 15.264 Å, as a function of temperature. The observed ratios, after being reduced by 10% for the Fe^{15+} contribution (Sec. 3), are represented in the figure by the horizontal lines. For these ratios the peak heights are used instead of the total flux in order to reduce the errors due to blending. The ratios indicate electron temperatures of 510 eV and 600 eV.

4.2 Electron Density

The possibilities for electron density diagnostics with the iron L-shell x-ray lines at high coronal temperatures are even more scarce than those for the electron temperature. We have employed a full collisional-radiative model for all of the iron ions Fe^{15+} - Fe^{21+} to obtain spectra calculated at the same temperature (600 eV) and ionization balance conditions, but for densities that differ by four orders of magnitude, from 10^9 through 10^{13} cm^{-3} . The calculated spectra are all found to be essentially identical to the total spectrum displayed in Figs. 2 and 3 for 600 eV.

Instead of the L-shell iron lines, one can use the He-like (K-shell) lines of lighter elements for relatively accurate density diagnostics. Such methods have been recently employed for the He-like C, N, and O lines in the Capella x-ray spectrum measured with the LETG spectrometer on board Chandra to yield densities between 10^9 and 10^{10} cm^{-3} (Brinkman et al. 2000). However, the He-like lines from these low-Z elements largely come from coronal regions that are significantly cooler than those from which the iron L-shell lines are emitted. On the other hand, Dupree et al. (1993) and Linsky et al. (1998) have used for density diagnostics EUV lines ($\Delta n = 0$) that are emitted by the same iron ions investigated in the present x-ray analysis. The electron density obtained from those EUV observations is about 10^{12} cm^{-3} and is probably more adequate for describing the present iron L-shell plasma than the low-Z K-shell densities.

4.3 Fractional Ion Abundances

The fractional abundances of the iron ions, which are obtained here from the comparison between the calculated and the observed spectra for Fe^{15+} - Fe^{21+} are: 0.06, 0.34, 0.25, 0.13, 0.11, 0.06, and 0.05, respectively, with an uncertainty of about 20%. The abundances of iron ions with $q < 15$ and $q > 21$ are negligible. In Fig. 5, the derived abundances are compared with recent ionization balance calculations by Mazzotta et al. (1998) for temperatures of 430 eV, 610 eV, and 860 eV. The observationally deduced values for Capella in the figure (squares) are given error bars of 20% in order to account for the uncertainties in the observed and calculated line intensities. Note that the calculated Fe^{15+} abundance at 860 eV, as well as the Fe^{20+} and Fe^{21+} abundances at

430 eV, are too low to be plotted in the scale of Fig. 5. It can be seen that the present values derived for Capella are in very good agreement with the calculated values for 610 eV, especially for the ions that dominate the spectrum, Fe^{16+} to Fe^{19+} . The calculated value for Fe^{16+} at 610 eV falls right on top of the measured data point and is barely seen in the figure. The temperature of about 600 eV indicated by the comparison with the ionization balance calculations is also in surprisingly good agreement with the value derived from the line ratios in the previous section. The ionization balance is much more sensitive to the electron temperature than the line ratios within any given charge state. This is well illustrated in Fig. 5 by the agreement of the observed abundances with those calculated for 610 eV as opposed to the complete disagreement with the calculations for 430 eV and 860 eV. On the other hand, the ionization balance calculations are not as reliable as the single ion theoretical spectra, the most questionable component in the ionization balance computations being the total dielectronic recombination rate coefficients. The fact that the empirically derived charge distribution is consistent with a single temperature is another indication that even if the iron-L emitting regions in the Capella coronae are not entirely isothermal, they are certainly characterized by a very narrow differential emission measure that sharply peaks around a temperature of about 600 eV.

5. VOLUME EMISSION MEASURE

The results of our coronal models for the various iron ionization states together with the measured flux in the present observation can be exploited to obtain a rough estimation of the volume emission measure VEM and subsequently the volume V of the emitting plasma. The VEM is obtained from the measured photon flux f , i.e., the number of photons detected per second and per cm^2 , and from the calculated number emissivity F , i.e., the number of photons emitted in the plasma per second and per cm^3 , through the relationship:

$$VEM = n_e^2 V = n_e^2 \frac{4\pi d^2 f}{F} \quad (3).$$

This form of the VEM assumes that there is no x-ray absorption and that all of the x-rays are emitted outward from the stars. The distance to Capella is denoted by d . The number emissivity F , which is directly obtained from the model, can be expressed as a sum over all of the photon emissions from excited levels j in all of the various charge states $q+$ of the ions in the plasma:

$$F = \sum_q \sum_{j,i} n_j^{q+} A_{ji} \quad (4).$$

The sum in eq. (4) is carried out only over those transitions that produce photons in the measured 10 - 18 Å wavelength band. In the atomic-state model we actually calculate the relative level populations n_j^{q+} / n^{q+} , where n^{q+} represents the total (summed over all of the levels of the ion) number density of $q+$ ions. This can be easily related to F by writing:

$$n_j^{q+} = n_e \frac{n_H}{n_e} \frac{n_{Fe}}{n_H} \frac{n_j^{q+}}{n_{Fe}} \frac{n_j^{q+}}{n^{q+}} \quad (5)$$

and hence:

$$F = n_e \frac{n_H}{n_e} \frac{n_{Fe}}{n_H} \sum_q \frac{n^{q+}}{n_{Fe}} \sum_{j,i} \frac{n_j^{q+}}{n^{q+}} A_{ji} \quad (6).$$

The sum on the extreme right hand side of eq. (6), $\sum(n_j^{q+} / n^{q+})A_{ji}$, is directly calculated in the model. The ionic fractional abundances n^{q+} / n_{Fe} are obtained, as described above, by fitting the calculated spectrum to the observed spectrum and by giving the appropriate weights to the various charge states. In the coronal approximation, the value of n_e^2/F , which is used for the *VEM* in eq. (3), is independent of the electron density assumed in the model. Standard solar values are used for the ratios n_H / n_e and n_{Fe} / n_H . For a fully ionized plasma comprised of 90% hydrogen and 10% helium, $n_H / n_e = 0.83$. Following Feldman (1992), n_{Fe} / n_H is taken to be 3.2×10^{-5} . All of the values needed for calculating the *VEM* from the current observation, corresponding to the 10 – 18 Å wavelength range, are summarized in Table II. Finally, by using all of these quantities in eq. (3), one obtains a *VEM* ($n_e^2 V$) of $2 \times 10^{53} \text{ cm}^{-3}$ for the x-ray iron-L emitting regions of Capella. Although this *VEM* is somewhat high, considering the many assumptions and estimated values involved in the calculation of the *VEM*, it is in reasonable agreement with the previously published x-ray *VEM* values for Capella of $9.5 \times 10^{52} \text{ cm}^{-3}$ (Mewe et al. 1982), $6.3 \times 10^{52} \text{ cm}^{-3}$ (Vedder & Canizares 1983), and $7.2 \times 10^{52} \text{ cm}^{-3}$ (Favata et al. 1997). The *VEM* values measured with the EUV lines (Dupree et al. 1993 & Linsky et al. 1998) are slightly lower, about $4 \times 10^{52} \text{ cm}^{-3}$ and below.

If the electron density is known, the volume of the emitting plasma can be calculated from the *VEM*. For electron densities of 10^{10} or 10^{12} cm^{-3} , we get volumes of 2×10^{33} or $2 \times 10^{29} \text{ cm}^3$, respectively. Assuming that the iron L-shell x-rays are emitted from (thin) layers, associated with a width w , around each of the two stars (coronae), we can write for V :

$$V = 8\pi R_*^2 w \quad (7),$$

where R_* is the average radius of the stars. For Capella, $R_* = 7.4 \times 10^{11} \text{ cm}$ (Hummell et al. 1994) and the average width is therefore 1.6×10^8 or $1.6 \times 10^4 \text{ cm}$, for respective densities of 10^{10} and 10^{12} cm^{-3} . These very small widths correspond to $2 \times 10^{-4} R_*$ or $2 \times 10^{-8} R_*$, which is lower than the $10^{-3} R_*$ estimation by Dupree et al. (1993).

CONCLUSIONS

It is shown that the x-ray line emission of Capella in the 10 – 18 Å wavelength range can be explained by means of a simple coronal model for the Fe^{15+} to Fe^{21+} ions. It is also shown that the observed iron spectrum can be characterized by one electron temperature and one electron density. By employing the detailed level-by-level

calculations, all of the iron lines in this wavelength range can be identified. Furthermore, the iron line intensities calculated for 600 eV and 10^{10} cm^{-3} agree, in most cases, with the observed intensities to within the observational uncertainties (20%). The relatively large discrepancy of 30% between the observed intensity ratio of the strong line at 15.015 Å to the line at 15.264 Å and its calculated value is mostly attributed to inaccuracy in the calculated value and to blending with the Fe^{15+} line at 15.264 Å, but it also may be affected by self-absorption of the 15.015 Å line. Line absorption will soon be incorporated in our collisional-radiative model in a self-consistent manner, by including its influence on the level populations as well as on the escape of radiation from the plasma. The model can then be used to determine the importance of self-absorption processes on the Capella plasma as well as for other stellar coronae.

Using the intensities of lines corresponding to the 2s-3p and 2p-4d transitions in Fe^{16+} , an electron temperature of about 500 - 600 eV is measured. The comparison between the fractional ion abundances, which are derived from the spectrum, and those obtained from ionization balance calculations in the literature also yields a temperature of about 600 eV. It is demonstrated that the iron lines in the wavelength range considered here do not show any sensitivity to the electron density and thus cannot be useful for density diagnostics. Finally, a volume emission measure of $2 \times 10^{53} \text{ cm}^{-3}$ is calculated for the iron-L emitting regions of the Capella coronae.

REFERENCES

- Arnaud, M., & Raymond, J. 1992, ApJ, 398, 394
- Bar-Shalom, A., Klapisch, M., & Oreg, J. 1988, Phys. Rev. A, 38, 1733
- Bar-Shalom A., Klapisch M., Goldstein W.H., & Oreg J. 1998, *The HULLAC code for atomic physics*, unpublished.
- Bauer, F., & Bergman, J.N. 1996, ApJ, 457, 382
- Brickhouse, N.S., & Drake, J.J. 1999, in the proceedings of *Astrophysical Plasmas: Codes, Models & Observations*, ed. S.J. Arthur, N.S. Brickhouse, & J. Franco (Mexico City).
- Brinkman, A.C., et al. 2000, preprint (astro-ph/0001034)
- Brown, G.V., Beiersdorfer, P., Liedahl, D.A., Widmann, K., & Kahn, S.M. 1998, ApJ, 502, 1015
- Brown, G.V., Beiersdorfer, P., Liedahl, D.A., Widmann, K., & Kahn, S.M. 2000, LLNL preprint (UCRL-JC-136647)
- Catura, R.C., Acton, L.W., & Johnson, H.M. 1975, ApJ, 196, L47
- Drake, G.W. 1988, Can. J. Phys., 66, 586
- Dupree, A.K., Brickhouse, N.S., Doschek, G.A., Green, J.C., & Raymond, J. 1993, ApJ, 418, L41
- Favata, F., Mewe, R., Brickhouse, N.C., Pallavicini, R., Micela, G., & Dupree, A.K. 1997, A&A, 324, L37
- Feldman, U., & Doschek, G.A. 1978, A&A 65, 215
- Feldman, U., Doschek, G.A., & Kreplin, R.W. 1982, ApJ, 260, 885
- Feldman, U. 1992, Phys. Scr., 46, 202
- Hummel, C.A., Armstrong, J.T., Quirrenbach, A., Buscher, D.F., Mozurkewich, D., & Elias, N.M. 1994, Astron. J., 107, 1859
- Klapisch, M. 1971, Comput. Phys. Commun. 2, 239
- Klapisch, M., Schwob, J.L., Fraenkel, B., & Oreg, J. 1977, J. Opt. Soc. Am. 67, 148
- Lemen, J.R., Mewe, R., Schrijver, C.J., & Fludra, A. 1989, ApJ, 341, 474
- Linsky, J.L., Wood, B.E., Brown, A., & Osten, R.A. 1998, ApJ, 492, 767
- Markert, T.H., Canizares, C.R., Dewey, D., McGuirk, M., Pak, C., & Schattenburg, M.L. 1995, Proc. SPIE, 2280, 168.
- Mazzotta, P., Mazzitelli, G., Colafrancesco, S., & Vittorio, N. 1998, A&AS, 133, 403
- McKenzie, D.L., Landecker, P.B., Broussard, R.M., Rugge, H.R., Young, R.M., Feldman, U., & Doschek, G.A. 1980, ApJ, 241, 409
- Mewe, R., et al. 1982, ApJ, 260, 233
- Raymond, J., & Smith, B.W. 1986, ApJ, 306, 762
- Schulz, N.S., Taylor, S.C., Dewey, D., & Marshall, H.L., available at <http://space.mit.edu/HETG/xrcf.html>
- Vedder, P.W. & Canizares, C.R. 1983, ApJ, 270, 666
- Waljeski, K., Moses, D., Dere, K.P., Saba, J.L.R., Web, D.F., & Zarro, D.M. 1994, ApJ, 429, 909

Table Captions:

Table I

The Capella spectral lines in the 10 - 18 Å wavelength range. Labels refer to the peaks of the observed spectrum in Figs. 1a and 1b. For each line, the observed wavelength $\lambda_{\text{observed}}$, the solar wavelength λ_{Sun} from McKenzie et al. (1980), the laboratory measured wavelength λ_{EBIT} from Brown et al. (1998, 2000), and the presently calculated wavelength λ_{HULLAC} are given. The upper and lower configurations of each transition are given together with the corresponding quantum numbers for the total angular momenta, J_U and J_L .

Table II

Quantities used for calculating the volume emission measure of the emitting plasma. See definitions in text.

Figure Captions:

Figure 1:

Observed Capella spectrum (top) obtained by the HETG spectrometer using the MEG grating. Positive and negative first orders have been summed. Labels correspond to the line identifications in Table I. The calculated iron spectrum is plotted at the bottom in arbitrary units, for comparison.

Figure 2:

Observed Capella spectrum (top) compared to the total calculated spectrum. The seven separate plots at the bottom of the figure show the individual-ion contributions of Fe^{15+} to Fe^{21+} . The spectra are calculated assuming plasma conditions of $kT_e = 600$ eV and $n_e = 10^{10} \text{ cm}^{-3}$. The lines are given a uniform Gaussian shape with 15 mÅ FWHM. The non-iron lines and blends are indicated by the numbers 1-3, corresponding, respectively, to lines from Ne, Ni, and O.

Figure 3:

Observed Capella spectrum (top) compared to total spectra calculated for $n_e = 10^{10} \text{ cm}^{-3}$, but for varying temperatures, $kT_e = 200$ eV, 600 eV, and 1000 eV. The ionic fractional abundances used for Fe^{15+} through Fe^{21+} are: 0.06, 0.34, 0.25, 0.13, 0.11, 0.06, and 0.05, respectively.

Figure 4:

Temperature sensitive intensity ratios of the Fe^{16+} lines at 13.829 Å (2s-3p) and 12.265 Å (2p-4d) to the Fe^{16+} line at 15.264 Å (2p-3d). The observed ratios, reduced by 10% to account for the Fe^{15+} contribution at 15.264 Å (see Sec. 3), are indicated by the horizontal lines. The calculated values were obtained by a coronal model at $n_e = 10^{10} \text{ cm}^{-3}$, including high Rydberg levels up to $n = 12$.

Figure 5:

Fractional abundances of iron ions Fe^{15+} through Fe^{21+} . The squares (with 20% error bars) indicate the values derived from the Capella observation. The triangles, circles, and diamonds represent the calculated values of Mazzotta et al. (1998) for 430 eV, 610 eV, and 860 eV, respectively. Lines are drawn between the data points to guide the eye. The Fe^{15+} abundance at 860 eV as well as the Fe^{20+} and Fe^{21+} abundances at 430 eV are too low to be seen.

Table I

Label	$\lambda_{\text{observed}}$ (Å)	λ_{Sun} (Å)	λ_{EBIT} (Å)	λ_{HULLAC} (Å)	Ion	Upper Configuration	J_U	Lower Configuration	J_L	Flux ($10^{-4} \text{s}^{-1} \text{cm}^{-2}$)
1	10.240	10.256		10.238	Ne ⁹⁺	3p _{3/2}	3/2	1s	1/2	2.64
				10.239	Ne ⁹⁺	3p _{1/2}	1/2	1s	1/2	
2	10.643	10.636		10.642	Fe ¹⁸⁺	2p _{1/2} 2p _{3/2} ² 4d _{3/2}	2	2p _{1/2} ² 2p _{3/2} ²	2	2.56
				10.649	Fe ¹⁸⁺	2p _{1/2} 2p _{3/2} ² 4d _{3/2}	3	2p _{1/2} ² 2p _{3/2} ²	2	
			10.657	10.669	Fe ¹⁶⁺	2p _{1/2} 2p _{3/2} ⁴ 6d _{3/2}	1	2p _{1/2} ² 2p _{3/2} ⁴	0	
3	10.768	10.778	10.770	10.782	Fe ¹⁶⁺	2p _{1/2} ² 2p _{3/2} ³ 6d _{5/2}	1	2p _{1/2} ² 2p _{3/2} ⁴	0	2.15
4	10.818	10.826	10.816	10.827	Fe ¹⁸⁺	2p _{1/2} 2p _{3/2} ² 4d _{5/2}	3	2p _{1/2} ² 2p _{3/2} ²	2	2.04
5	10.996	10.990		11.009	Ne ⁸⁺	1s4p _{3/2}	1	1s ²	0	1.89
6	11.022	11.031	11.026	10.012	Fe ¹⁶⁺	2s2p _{1/2} ² 2p _{3/2} ⁴ 4p _{3/2}	1	2s ² 2p _{1/2} ² 2p _{3/2} ⁴	0	1.52
7	11.129	11.140	11.131	11.142	Fe ¹⁶⁺	2p _{1/2} 2p _{3/2} ⁴ 5d _{3/2}	1	2p _{1/2} ² 2p _{3/2} ⁴	0	2.03
8	11.251	11.255	11.254	11.262	Fe ¹⁶⁺	2p _{1/2} ² 2p _{3/2} ³ 5d _{5/2}	1	2p _{1/2} ² 2p _{3/2} ⁴	0	2.64
9	11.323	11.336	11.326	11.332	Fe ¹⁷⁺	2p _{1/2} 2p _{3/2} ³ 4d _{3/2}	5/2	2p _{1/2} ² 2p _{3/2} ³	3/2	2.76

	11.326	11.336	Fe ¹⁷⁺	2p _{1/2} 2p _{3/2} ³ 4d _{5/2}	3/2	2p _{1/2} ² 2p _{3/2} ³	3/2	
10	11.424	11.445	11.423	11.435	Fe ¹⁷⁺	2p _{1/2} 2p _{3/2} ³ 4d _{3/2}	5/2	2p _{1/2} ² 2p _{3/2} ³ 2.74
11	11.529	11.537	11.527	11.537	Fe ¹⁷⁺	2p _{1/2} ² 2p _{3/2} ² 4d _{5/2}	5/2	2p _{1/2} ² 2p _{3/2} ³ 3.61
12	11.544	11.537		11.554	Ne ⁸⁺	1s3p _{3/2}	1	1s ² 0 2.94
13	11.742	11.742	11.736	11.758	Fe ²²⁺	2s3d _{5/2}	2	2s2p _{3/2} 1 1.36
14	11.770	11.770	11.770	11.780	Fe ²¹⁺	3d _{3/2}	3/2	2p _{1/2} 1/2 1.53
15	12.131	12.127	12.124	12.135	Fe ¹⁶⁺	2p _{1/2} 2p _{3/2} ⁴ 4d _{3/2}	1	2p _{1/2} ² 2p _{3/2} ⁴ 0 20.6
				12.132	Ne ⁹⁺	2p _{3/2}	3/2	1s 1/2
				12.137	Ne ⁹⁺	2p _{1/2}	1/2	1s 1/2
16	12.266	12.276	12.266	12.272	Fe ¹⁶⁺	2p _{1/2} ² 2p _{3/2} ³ 4d _{5/2}	1	2p _{1/2} ² 2p _{3/2} ⁴ 0 7.40
17	12.286	12.276	12.284	12.295	Fe ²⁰⁺	2p _{1/2} 3d _{3/2}	1	2p _{1/2} ² 0
18	12.404	12.401		12.405	Fe ¹⁵⁺	2p _{1/2} ² 2p _{3/2} ³ 3s4d _{3/2}	5/2	2p _{1/2} ² 2p _{3/2} ⁴ 3s 1/2
			12.393	12.404	Fe ²⁰⁺	2p _{1/2} 3d _{3/2}	1	2p _{1/2} 2p _{3/2} 1
19	12.431	12.428		12.431	Ni ¹⁸⁺	2p _{1/2} 2p _{3/2} ⁴ 3d _{3/2}	1	2p _{1/2} ² 2p _{3/2} ⁴ 0 4.14
20a	12.550			12.547	Fe ¹⁵⁺	2p _{1/2} ² 2p _{3/2} ³ 3s4d _{5/2}	3/2	2p _{1/2} ² 2p _{3/2} ⁴ 3s 1/2

20b	12.571	12.583	12.576	12.604	Fe ¹⁹⁺	2s2p _{1/2} 2p _{3/2} ² 3p _{1/2}	3/2	2s ² 2p _{1/2} ² 2p _{3/2}	3/2
21	12.651	12.657		12.659	Ni ¹⁸⁺	2p _{1/2} ² 2p _{3/2} ³ 3d _{5/2}	1	2p _{1/2} ² 2p _{3/2} ⁴	0
22	12.822	12.832	12.824	12.820	Fe ¹⁹⁺	2p _{1/2} 2p _{3/2} 3d _{3/2}	1/2	2p _{1/2} ² 2p _{3/2}	3/2
23	12.846	12.832	12.846	12.835	Fe ¹⁹⁺	2p _{1/2} 2p _{3/2} 3d _{3/2}	3/2	2p _{1/2} ² 2p _{3/2}	3/2
		12.832	12.864	12.854	Fe ¹⁹⁺	2p _{1/2} 2p _{3/2} 3d _{5/2}	5/2	2p _{1/2} ² 2p _{3/2}	3/2
24	12.930	12.926	12.915	12.912	Fe ¹⁹⁺	2p _{1/2} 2p _{3/2} 3d _{5/2}	5/2	2p _{1/2} ² 2p _{3/2}	3/2
25	12.953	12.953	12.965	12.960	Fe ¹⁹⁺	2p _{1/2} 2p _{3/2} 3d _{3/2}	5/2	2p _{1/2} ² 2p _{3/2}	3/2
26a	13.138	13.146	13.137	13.153	Fe ¹⁹⁺	2p _{1/2} 2p _{3/2} 3d _{5/2}	5/2	2p _{1/2} ² 2p _{3/2} ²	3/2
26b	13.155	13.166	13.153	13.163	Fe ¹⁹⁺	2p _{1/2} 2p _{3/2} 3d _{5/2}	5/2	2p _{1/2} ² 2p _{3/2} ²	5/2
27	13.449	13.450		13.450	Ne ⁸⁺	1s2p _{3/2}	1	1s ²	0
28	13.455	13.450	13.462	13.475	Fe ¹⁸⁺	2p _{1/2} 2p _{3/2} ² 3d _{3/2}	1	2p _{1/2} ² 2p _{3/2} ²	2
29	13.465	13.450	13.462	13.475	Fe ¹⁸⁺	2p _{1/2} 2p _{3/2} ² 3d _{3/2}	1	2p _{1/2} ² 2p _{3/2} ²	0
30	13.518	13.517	13.518	13.525	Fe ¹⁸⁺	2p _{1/2} ² 2p _{3/2} 3d _{5/2}	3	2p _{1/2} ² 2p _{3/2} ²	2
31	13.550			13.569	Ne ⁸⁺	1s2p _{1/2}	1	1s ²	0
				13.551	Fe ¹⁸⁺	2p _{3/2} ³ 3p _{3/2}	2	2p _{1/2} ² 2p _{3/2} ²	2

32	13.649	13.651	13.645	13.658	Fe ¹⁸⁺	2p _{1/2} 2p _{3/2} ² 3d _{3/2}	3	2p _{1/2} ² 2p _{3/2} ²	2	3.02
33	13.701	13.701		13.715	Ne ⁸⁺	1s2s	1	1s ²	0	9.79
34a	13.783	13.791		13.793	Ni ¹⁸⁺	2p _{1/2} 2p _{3/2} ⁴ 3s	1	2p _{1/2} ² 2p _{3/2} ⁴	0	4.42
34b	13.797		13.795	13.807	Fe ¹⁸⁺	2p _{1/2} 2p _{3/2} ² 3d _{5/2}	3	2p _{1/2} ² 2p _{3/2} ²	2	4.49
35	13.829	13.847	13.825	13.793	Fe ¹⁶⁺	2s2p _{1/2} ² 2p _{3/2} ⁴ 3p _{3/2}	1	2p _{1/2} ² 2p _{3/2} ⁴	0	9.85
36	13.888		13.892	13.859	Fe ¹⁶⁺	2s2p _{1/2} ² 2p _{3/2} ⁴ 3p _{1/2}	1	2p _{1/2} ² 2p _{3/2} ⁴	0	1.96
37a	13.932		13.934	13.952	Fe ¹⁸⁺	2p _{1/2} 2p _{3/2} ² 3d _{5/2}	1	2p _{1/2} ² 2p _{3/2} ²	0	1.85
37b	13.950	13.947	13.956	13.954	Fe ¹⁸⁺	2p _{1/2} 2p _{3/2} ² 3d _{3/2}	2	2p _{1/2} ² 2p _{3/2} ²	2	
37c	13.975	13.967	13.953	13.979	Fe ¹⁷⁺	2p _{3/2} ⁴ 3d _{5/2}	5/2	2p _{1/2} ² 2p _{3/2} ³	3/2	
38	14.041	14.025	14.034	14.027	Fe ¹⁸⁺	2p _{1/2} ² 2p _{3/2} 3d _{5/2}	2	2p _{1/2} 2p _{3/2} ³	1	4.56
		14.037		14.056	Ni ¹⁸⁺	2p _{1/2} ² 2p _{3/2} ³ 3s	1	2p _{1/2} ² 2p _{3/2} ⁴	0	
39	14.080	14.082		14.092	Ni ¹⁸⁺	2p _{1/2} ² 2p _{3/2} ³ 3s	2	2p _{1/2} ² 2p _{3/2} ⁴	0	2.89
40	14.206	14.220	14.208	14.205	Fe ¹⁷⁺	2p _{1/2} 2p _{3/2} ³ 3d _{3/2}	5/2	2p _{1/2} ² 2p _{3/2} ³	3/2	22.1
			14.208	14.218	Fe ¹⁷⁺	2p _{1/2} 2p _{3/2} ³ 3d _{5/2}	3/2	2p _{1/2} ² 2p _{3/2} ³	3/2	

41	14.261	14.281	14.256	14.276	Fe ¹⁷⁺	$2p_{1/2}2p_{3/2}^33d_{3/2}$	1/2	$2p_{1/2}^22p_{3/2}^3$	3/2	6.94
42	14.374	14.388	14.373	14.387	Fe ¹⁷⁺	$2p_{1/2}2p_{3/2}^33d_{3/2}$	5/2	$2p_{1/2}^22p_{3/2}^3$	3/2	7.69
43	14.535		14.534	14.549	Fe ¹⁷⁺	$2p_{1/2}^22p_{3/2}^23d_{5/2}$	5/2	$2p_{1/2}^22p_{3/2}^3$	3/2	4.26
44	14.552	14.549	14.571	14.569	Fe ¹⁷⁺	$2p_{1/2}^22p_{3/2}^23d_{5/2}$	3/2	$2p_{1/2}^22p_{3/2}^3$	3/2	3.05
45	14.588		14.616	14.602	Fe ¹⁷⁺	$2p_{1/2}^22p_{3/2}^23d_{5/2}$	1/2	$2p_{1/2}^22p_{3/2}^3$	3/2	2.59
46	14.669	14.671	14.664	14.681	Fe ¹⁸⁺	$2p_{1/2}2p_{3/2}^23s$	3	$2p_{1/2}^22p_{3/2}^2$	2	2.57
47a	14.742	14.743	14.725	14.758	Fe ¹⁸⁺	$2p_{1/2}2p_{3/2}^23s$	2	$2p_{1/2}^22p_{3/2}^2$	2	
47b	14.755	14.759	14.754	14.776	Fe ¹⁹⁺	$2s^22p_{1/2}2p_{3/2}3p_{3/2}$	3/2	$2s2p_{1/2}^22p_{3/2}^2$	5/2	
48	14.905	14.919	14.910	14.924	Fe ¹⁷⁺	$2p_{1/2}^22p_{3/2}^23d_{3/2}$	3/2	$2p_{1/2}^12p_{3/2}^4$	1/2	2.08
49	14.969	14.962	14.961	14.986	Fe ¹⁸⁺	$2p_{1/2}^22p_{3/2}3s$	1	$2p_{1/2}^22p_{3/2}^2$	2	2.38
50	15.015	15.013	15.014	15.014	Fe ¹⁶⁺	$2p_{1/2}2p_{3/2}^43d_{3/2}$	1	$2p_{1/2}^22p_{3/2}^4$	0	60.0
51	15.082	15.083		15.095	Fe ¹⁵⁺	$2p_{1/2}2p_{3/2}^43s3d_{3/2}$	3/2	$2p_{1/2}^22p_{3/2}^43s$	1/2	7.19
52	15.181		15.175		O ⁷⁺	$4p_{3/2}$	3/2	1s	1/2	3.95
			15.176		O ⁷⁺	$4p_{1/2}$	1/2	1s	1/2	
53a	15.201	15.198	15.198	15.225	Fe ¹⁸⁺	$2s2p_{1/2}^22p_{3/2}^23s$	2	$2s2p_{1/2}^22p_{3/2}^3$	2	

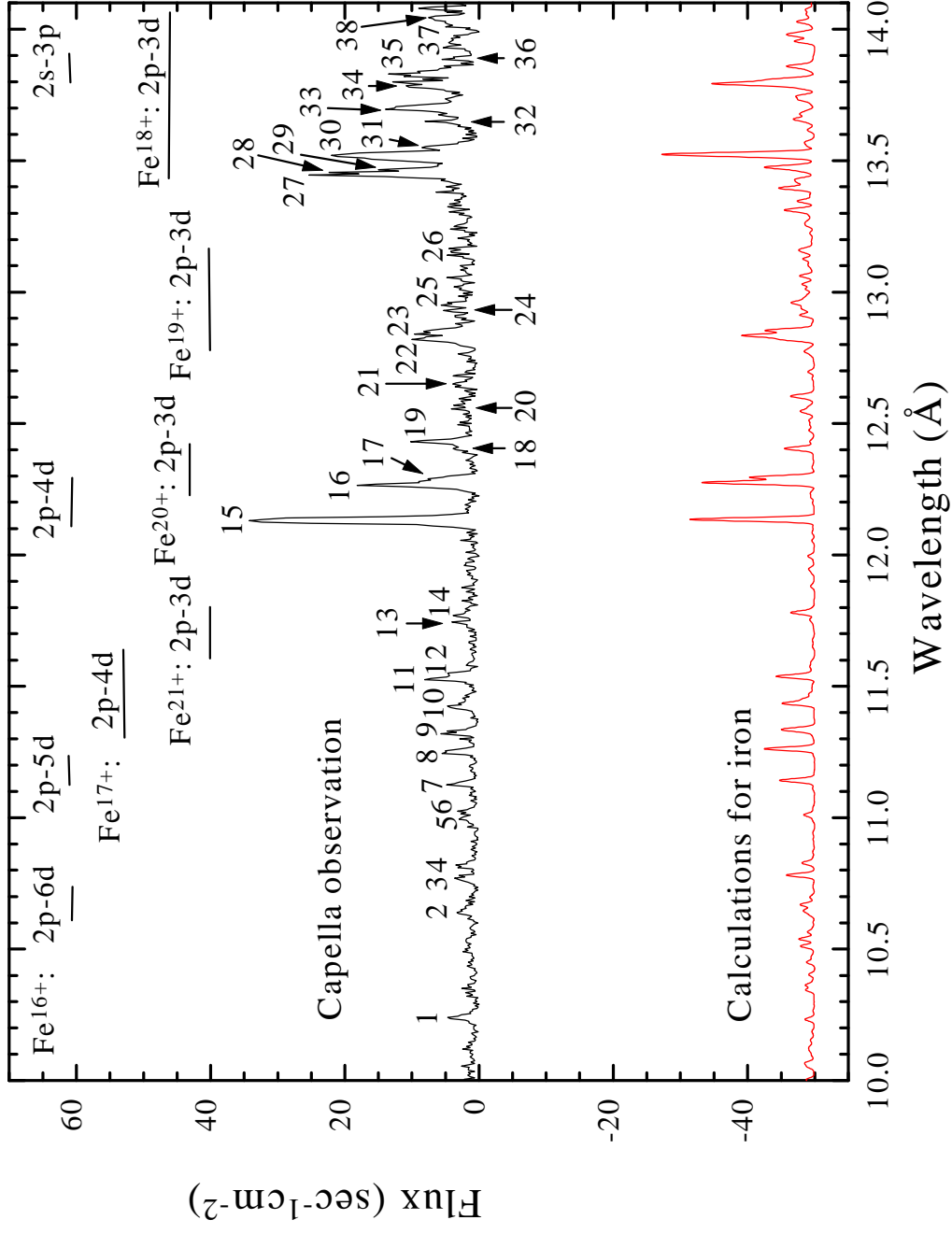
53b	15.210		15.203	Fe ¹⁵⁺	2p _{1/2} 2p _{3/2} ⁴ 3s3d _{3/2}	1/2	2p _{1/2} ² 2p _{3/2} ⁴ 3s	1/2	
54	15.264	15.262	--	Fe ¹⁵⁺	2p _{1/2} ² 2p _{3/2} ³ 3s3d _{5/2}	3/2	2p _{1/2} ² 2p _{3/2} ⁴ 3s	1/2	24.9
		15.261	15.272	Fe ¹⁶⁺	2p _{1/2} ² 2p _{3/2} ³ 3d _{5/2}	1	2p _{1/2} ² 2p _{3/2} ⁴	0	
55	15.454	15.456	15.470	Fe ¹⁶⁺	2p _{1/2} ² 2p _{3/2} ³ 3d _{3/2}	1	2p _{1/2} ² 2p _{3/2} ⁴	0	5.40
56	15.628	15.630	15.642	Fe ¹⁷⁺	2p _{1/2} 2p _{3/2} ³ 3s	5/2	2p _{1/2} ² 2p _{3/2} ³	3/2	8.06
57	15.827	15.827	15.854	Fe ¹⁷⁺	2p _{1/2} 2p _{3/2} ³ 3s	3/2	2p _{1/2} ² 2p _{3/2} ³	3/2	5.93
58	15.875	15.869	15.884	Fe ¹⁷⁺	2p _{1/2} 2p _{3/2} ³ 3s	3/2	2p _{1/2} 2p _{3/2} ⁴	1/2	6.82
59	16.008	16.004	16.005	O ⁷⁺	3p _{3/2}	3/2	1s	1/2	18.1
			16.006	O ⁷⁺	3p _{1/2}	1/2	1s	1/2	
		16.004	16.024	Fe ¹⁷⁺	2p _{1/2} ² 2p _{3/2} ² 3s	3/2	2p _{1/2} ² 2p _{3/2} ³	3/2	
60	16.078	16.070	16.098	Fe ¹⁷⁺	2p _{1/2} ² 2p _{3/2} ² 3s	5/2	2p _{1/2} ² 2p _{3/2} ³	3/2	19.2
61	16.111	16.108	16.132	Fe ¹⁸⁺	2s ² 2p _{1/2} 2p _{3/2} ² 3p _{1/2}	2	2s2p _{1/2} ² 2p _{3/2} ³	2	4.63
62	16.170	16.165	16.198	Fe ¹⁷⁺	2s2p _{1/2} 2p _{3/2} ⁴ 3s	3/2	2s2p _{1/2} ² 2p _{3/2} ⁴	1/2	4.45
63	16.779	16.775	16.796	Fe ¹⁶⁺	2p _{1/2} 2p _{3/2} ⁴ 3s	1	2p _{1/2} ² 2p _{3/2} ⁴	0	41.7
64	17.054	17.043	17.071	Fe ¹⁶⁺	2p _{1/2} ² 2p _{3/2} ³ 3s	1	2p _{1/2} ² 2p _{3/2} ⁴	0	5.03

65	17.099	17.084	17.096	17.118	Fe^{16+}	$2p_{1/2}^2 2p_{3/2}^3 3s$	2	$2p_{1/2}^2 2p_{3/2}^4$	0	48.5
66	17.625	17.617	17.623	17.674	Fe^{17+}	$2s^2 2p_{1/2} 2p_{3/2}^3 3p_{1/2}$	3/2	$2s 2p_{1/2}^2 2p_{3/2}^4$	1/2	7.64

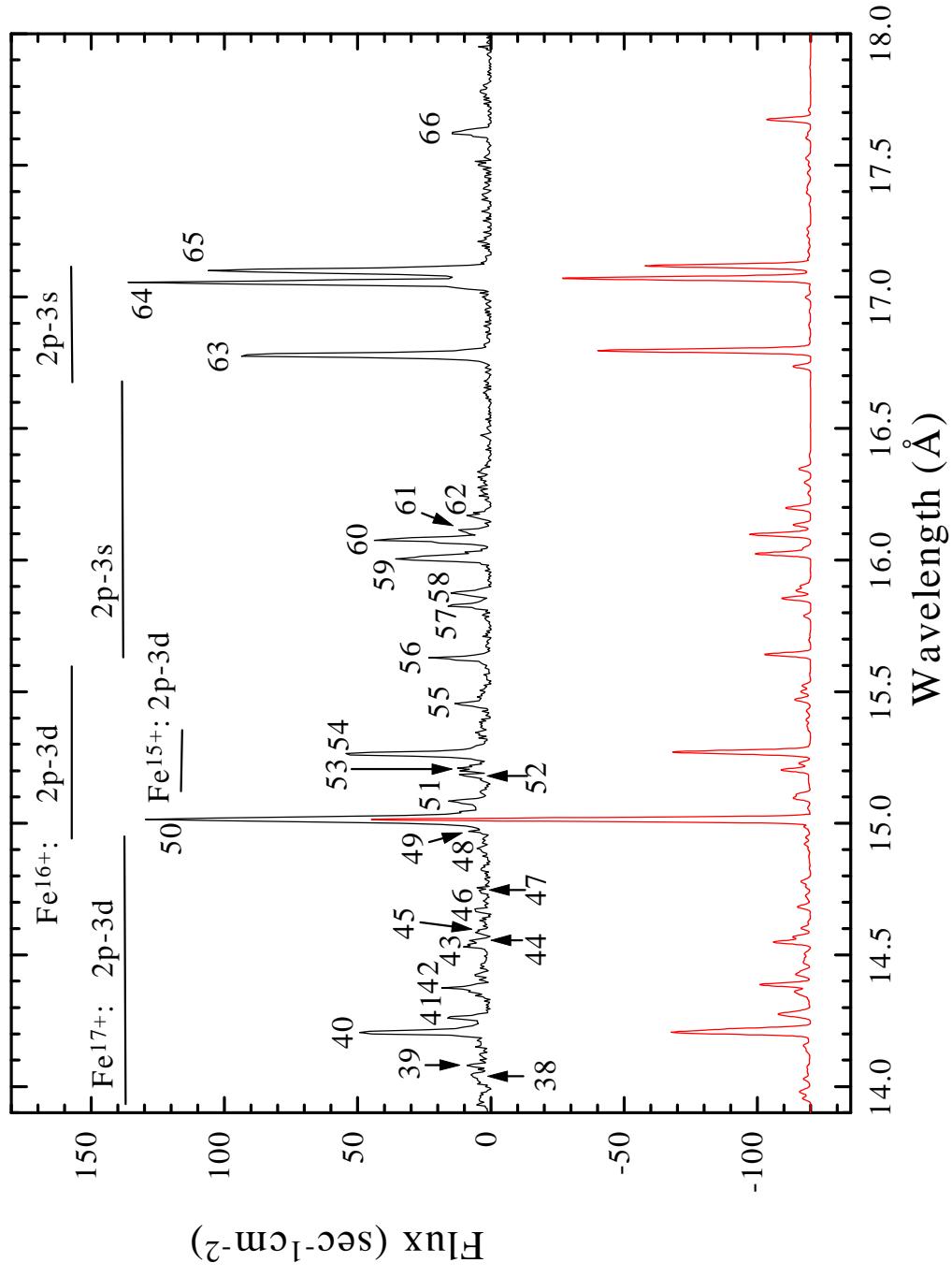
Table II

Quantity	Value	Obtained from:
f	0.073 (photons) sec ⁻¹ cm ⁻²	Observation
$\sum_q \frac{n^{q+}}{n_{Fe}} \sum_j \frac{n_j^{q+}}{n_j^{q+}} A_{ji}$	2.62 (photons) sec ⁻¹	The model (second sum) and fitting to observation
n_H / n_e	0.83	Solar standard
n_{Fe} / n_H	3.2×10 ⁻⁵	Feldman 1992, Solar value
F	6.96×10 ⁵ (photons)sec ⁻¹ cm ⁻³	Eq. (6)
d	13.3pc= 4.1×10 ¹⁹ cm	Hummel et al. 1994

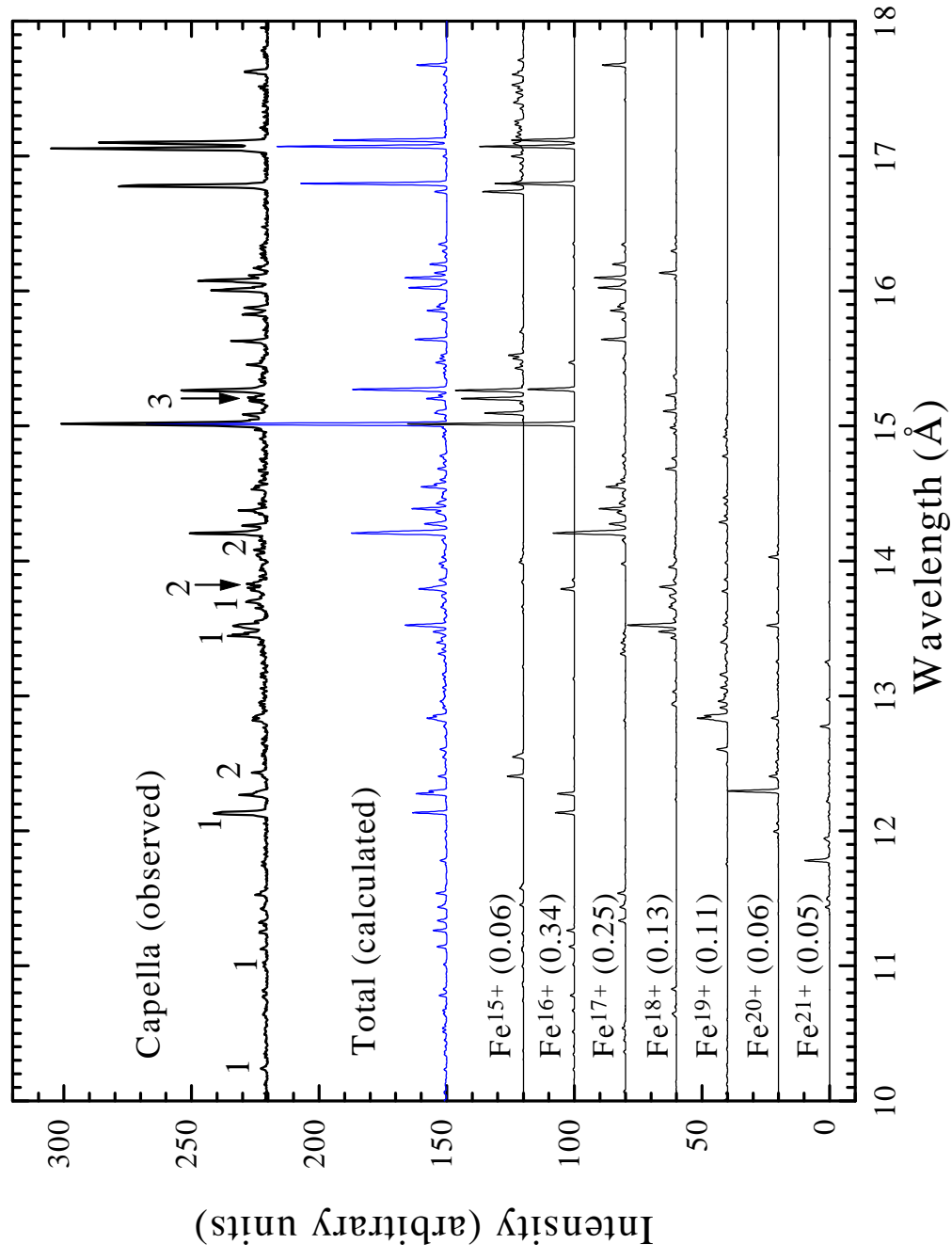
Behar et al. Fig. 1a



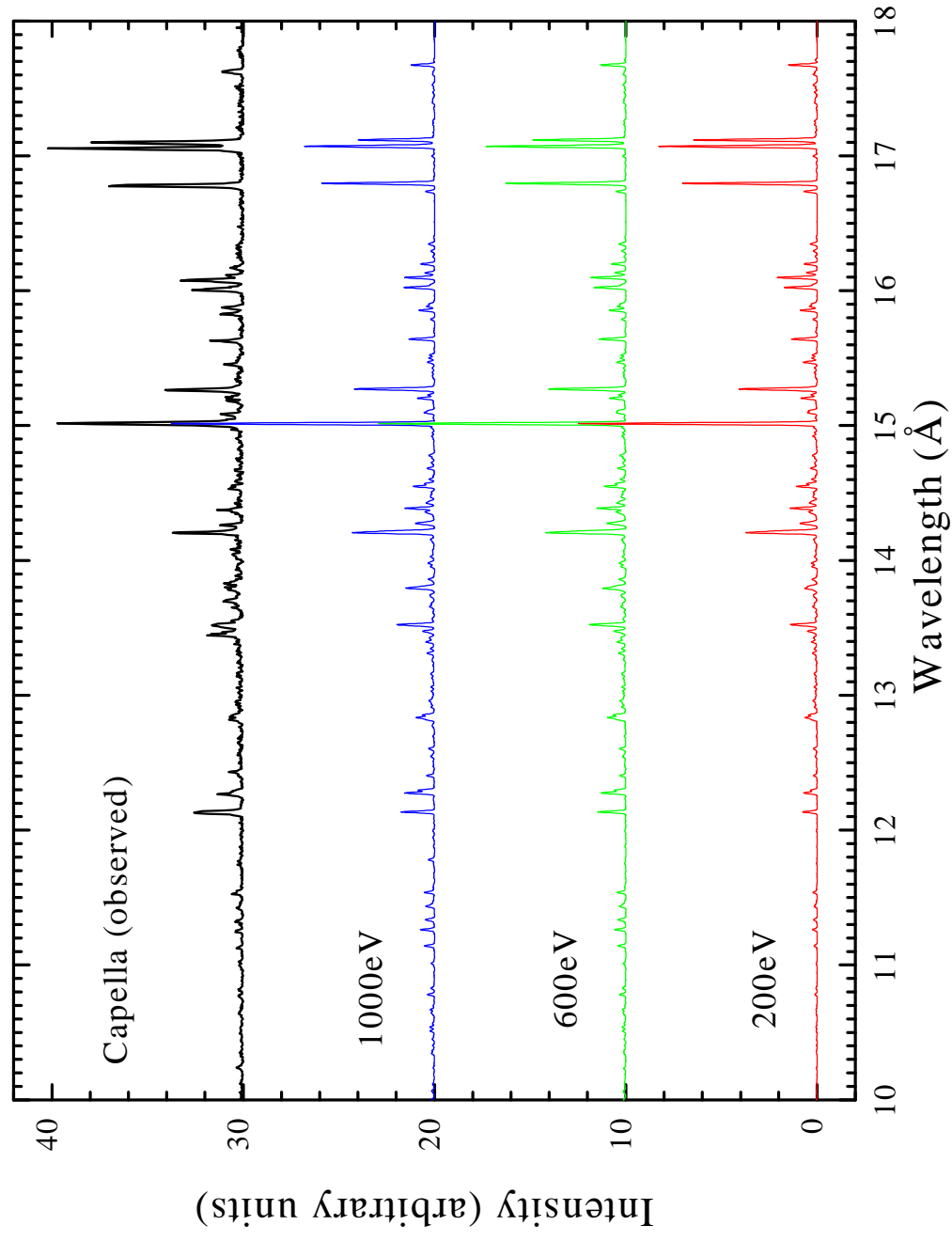
Behar et al. Fig. 1b



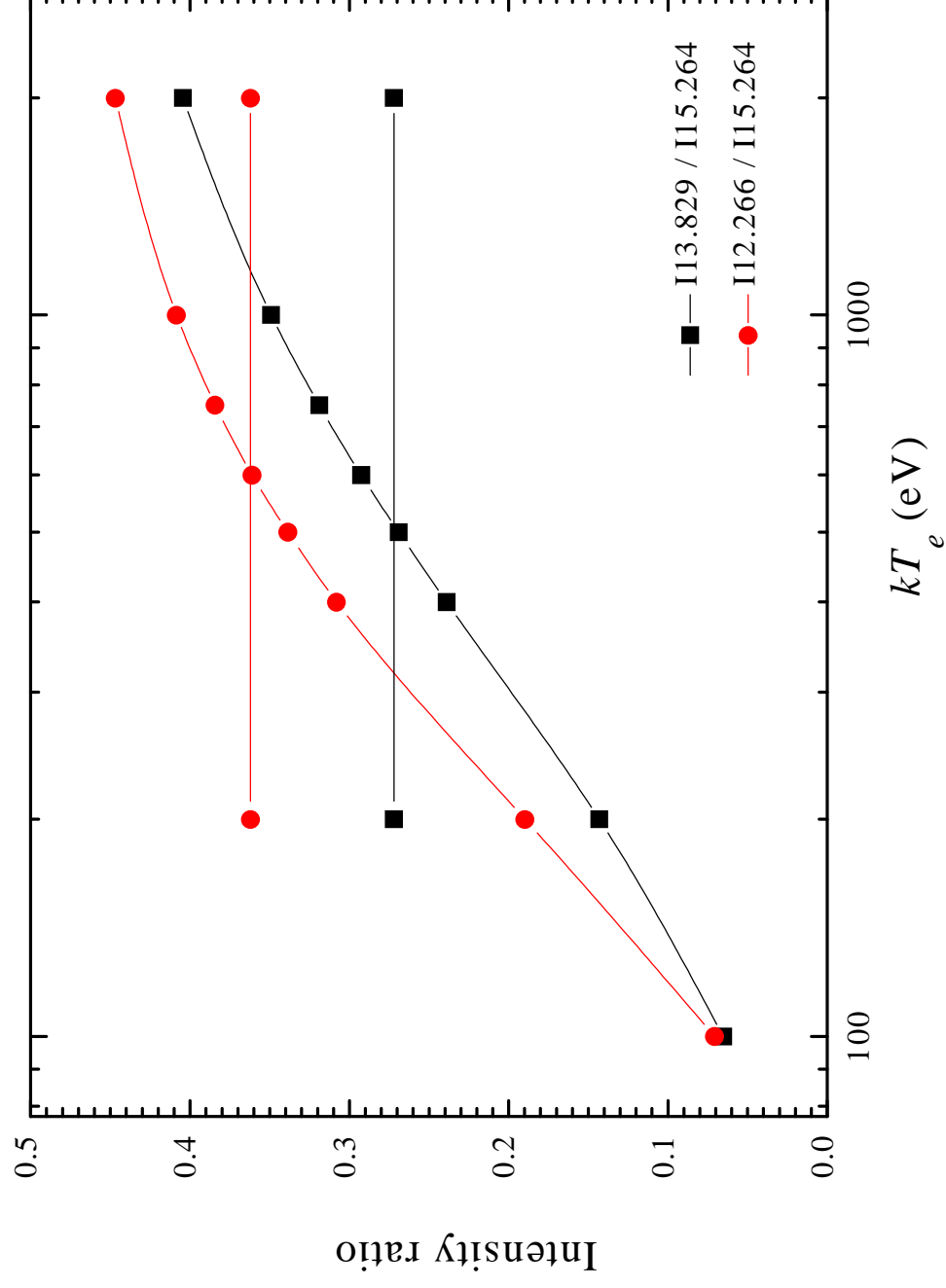
Behar et al. Fig. 2



Behar et al. Fig. 3



Behar et al. Fig. 4



Behar et al. Fig. 5

